GEOPHYSICS, VOL. 71, NO. 6 (NOVEMBER-DECEMBER 2006); P. B193–B199, 9 FIGS.
10.1190/1.2345193

Electrical and GPR prospecting at Palo Blanco archaeological site, northwestern Argentina

Luis Martino[1], Néstor Bonomo[1], Eugenia Lascano[2], Ana Osella[1], and Norma Ratto[3]

ABSTRACT

We conducted a geophysical survey at the Palo Blanco archaeological site located in Catamarca, Argentina. Age estimates from radiocarbon dating indicate first occupation of the site around 1500 years ago. The first description of the site was done in 1960. At that time, five residential units with different architectural arrangements were reported. These structures had different levels of deterioration caused by exposure and human activities. Some of these original structures have become completely covered by sediments. To aid in the design of efficient excavation plans, detailed maps are required to locate the buried walls. For this purpose, we conducted geophysical surveys over one of the structures. We had poor documentation about the structure at the time of the survey. Only one of the walls described in the earlier report was partially visible. We used two geophysical methods: ground-penetrating radar (GPR) and electrical resistivity. We performed 2D inversion of the resistivity data, together with numerical GPR simulations. These helped to distinguish the expected reflection events from others, aiding in a correct interpretation of the data. Finally, we made a complementary interpretation of the resistivity and GPR data to compile a detailed map of the selected structure. We found that considering the two methods independently would have led to an incomplete map. We delineated a much more complex structure than originally expected and designed an excavation plan which was carried out. The layout of the rooms of the structure fully matched the predictions based on the interpretation used in detecting the walls and their depths. In this way, the geophysical forecasts were confirmed after excavation.

INTRODUCTION

The archaeological site of Palo Blanco provides evidence of the development of the first agricultural/pastoral communities that settled in the northern part of the Fiambalá Valley (Catamarca, Argentina) (Figure 1a). The radiocarbon dating of in-situ samples indicates a long-term occupation between 1330 (±100) and 1760 (±95) years old (Gordillo, 1999), which correlates with the formative stage of the Catamarca area in the northwestern region of Argentina.

The first studies, begun in 1960 by M.C. Sempé, provide an approximate description of various buildings in Palo Blanco (Sempé, 1976, 1977). Sempé found a set of five structures with fence walls, each with a different architectural arrangement (Figure 1b). Each of these building units, named NH1 to NH5, consisted of three or four predominantly rectangle-shaped enclosures, which were also connected outdoors by means of narrow passageways that, in some cases, led to wider areas interpreted as yards. The preliminary description of the units' buildings inferred the existence of an architectural complexity, but it was recognized that a more intensive study would be required to make an adequate assessment of the characteristics of the site for analyzing the habits of the inhabitants (Hillier and Hanson, 1984; Blanton, 1994). In this context, archaeological researchers are in the process of compiling a precise map of the buildings to relate building usage to the sociospatial and technical characteristics during the development of the site.

Because of deterioration from exposure and human activities, the architectural features of Palo Blanco have very low or no surface visibility. Walls and other architectural features, found by Sempé in the middle 1960s, are presently covered by eolian deposits and/or are partially collapsed and mixed with the natural soil matrix. Geophysical methods provided an opportunity to define more precisely the characteristics of the housing clusters and to contribute to the excavation design of one of them, NH3 (Figure 1b). This structure was chosen because its architectural shape seemed to be very different from the others (with a smaller and seemingly simpler structure, as

Manuscript received by the Editor April 19, 2005; revised manuscript received February 7, 2006; published online October 3, 2006.
[1]Universidad de Buenos Aires, Departmentamento de Física, Facultad de Ciencias Exactas y Naturales, Ciudad Universitaria, Pabellón 1, (1428) Buenos Aires, Argentina and CONICET, Consejo Nacional de Investigaciones Científicas y Técnicas. E-mail: lmartino@df.uba.ar; bonomo@df.uba.ar; osella@df.uba.ar.
[2]Universidad de Buenos Aires, Departmentamento de Física, Facultad de Ciencias Exactas y Naturales, Ciudad Universitaria, Pabellón 1, (1428) Buenos Aires, Argentina.
[3]Universidad de Buenos Aires, Departamento de Arqueología, Facultad de Filosofía y Letras, Buenos Aires, Argentina.

shown in Figure 1b), and it had not been excavated. The survey of the NH3 structure cluster helped initiate the systematic excavation of other units not yet disrupted in Palo Blanco to study the development and causes of desertion, which had not been taken into consideration during the original investigations.

We needed a map of the NH3 cluster that showed the arrangement of the buried walls. Figure 2 is a photo of NH3 before the geophysical investigation of the area with the structure deduced from Sempé's report; only a part of the main wall could be seen at the surface. Two prospecting methods were used to map NH3: ground-penetrating radar (GPR) and dipole-dipole profiles. Both methods proved to give reliable results for mapping anomalies related to these kind of structures (Herbich et al., 1997; Ambos and Larson, 2002; Thacker and Ellwood, 2002; Osella et al., 2005). Because they complement each other, the joint application overcame intrinsic limitations of each method. For example, ancient walls usually present undefined interfaces caused by deterioration, so detection by GPR could fail in these cases. Analogously, the geoelectrical method could not detect very small differences in the resistivity. Furthermore, special care was required because the site is located in a dry region where mud flows or mudslides are common, which could give rise to responses similar to those caused by buried man-made structures. It is important to note that the people who settled in Palo Blanco usually built their walls with clay materials extracted from the surroundings. With the goal of reducing ambiguities, we employed numerical simulations and joint data interpretation, allowing us to construct a high-resolution map that was used as a reference for subsequent excavation.

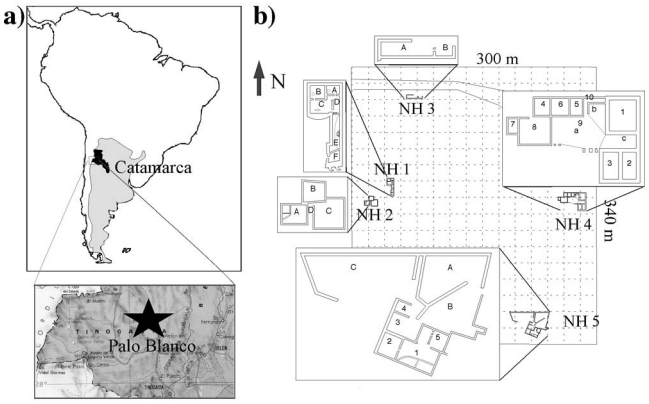

Figure 1. (a) Location of Palo Blanco archaeological site. (b) An interpretation of Sempé (1976) showing the probable locations for residential units NH1–NH5.

Figure 2. View of the study area delimited with dashed lines together with the outline of the NH3 house (solid line) as interpreted by Sempé (1976). An exposed wall is pointed out with the dotted lines. Point O indicates the origin of the orthogonal reference lines of the geophysical grid.

SITE DESCRIPTION

The site is located in the Fiambalá Valley, 1900 m above sea level. The valley is 50 km wide and flanked to the east and west by north-south-trending mountains with elevations greater than 3000 m. The climate is dry, with annual rainfall at the site below 100 mm. Large topographic changes and the dry weather result in sparse vegetation and a desert-like environment. The site is sparsely vegetated, and the desert soils have low organic content and are derived from sand and pumice fragments (see Figure 2).

Recent paleoenvironmental studies indicate that the dynamics of rivers in the region changed during the past 1000 years. Periods with intense water erosion shaped the riverbeds, defining differences in base levels up to 5 m. The NH3 structure is located near one of these rivers, hence topography varies across the sector with a moderate maximum difference of 1.2 m (Figure 3). The river near NH3, a channel of Ranchillos River, is now completely dry resulting from irrigation demands upstream. At present, the river channel is filled with eolian sand. It has been observed that elevation changes in NH3 seem to have originated before the site was active, probably as a result of a great overflow of Ranchillos River. Whether this was the reason for abandoning the community in the past is yet to be determined.

DIPOLE-DIPOLE RESISTIVITY SURVEY

For the purpose of obtaining a detailed description of the buried structures, a resistivity survey was carried out along the lines shown in Figure 3. We collected the data using the Scintrex automated resistivity imaging system (SARIS) multiple-electrode system. A total of 35 profiles was acquired: 23 in the south-north direction, called the "L" lines, and nine profiles in the east-west direction, called the "T" lines. We used the dipole-dipole configuration with 1-m dipoles and a maximum separation of $n = 8$. Three of the south-north profiles, L5, L6, and L7, were also acquired with 0.5-m dipoles to obtain better resolution in an area containing a wall.

The near surface is highly resistive, so much so that we had difficulty injecting current into the ground even for small dipole-dipole apertures. To decrease the potential barriers at the electrode-ground interface, we added water at the electrodes, which substantially

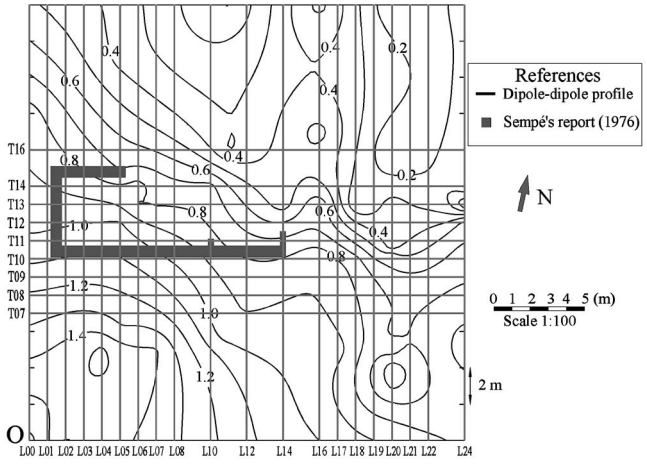

Figure 3. Diagram of the NH3 site, including topography (in meters). The gray lines correspond to the dipole-dipole profiles. The structures interpreted by Sempé (1966) are also shown. Point O indicates the origin of the reference lines, as in Figure 2.

helped the current input. To check that the data were not distorted by the wetting, we selected profiles that did not require the wetting at the current electrodes and compared this data with data acquired at the same profiles after adding water. The only two differences appeared at a few points corresponding to the first aperture. We also checked the depth of penetration of the signals. This preliminary analysis was done in the field using the inversion code of Loke and Barker (1996). The resulting 2D electrical images allowed us to determine that we had penetration of a minimum of 5 m, sufficient for the targets of interest.

For the final analysis of the data, including topographic corrections, we used the 2D inverse code of Oldenburg et al. (1993) and Oldenburg and Li (1994). For the 2D inversion of the data, a general global objective function is defined. This objective function has different terms, each with a weighting coefficient: one that depends on the recovered model unknown in the inversion problem and on a reference model supplied at run time, two terms that measure the difference between model and reference and the smoothness in either spatial direction, and a last term with the data misfit function. The inversion finds a model that minimizes the objective function subject to a determined misfit, i.e., the distribution of the difference between the observed and predicted data, normalized by the standard deviation. A measure of the quality of the inversion process is given by this parameter. We looked for mean values less than 5% for all the profiles. It should be noted that a low value for the misfit is not enough to guarantee the validity of the resulting model; it is well known that solutions of inversion problems are not unique, and different coefficients of the objective function can be adjusted to find models that are acceptable mathematically as well as geologically.

We also calculated the so-called depth of investigation of a profile (Oldenburg and Li, 1999). By inverting the data with different inputs and comparing the resulting images, we estimated the depth to which the resulting models are independent of the initial parameters. In this way, we could determine which part of the model obtained from the inversion of the field data reliably represents the subsoil. We followed this procedure for each profile to determine the depth to which the models were reliable.

As an example, Figure 4 shows the results of the inversion of data acquired along five south-north-directed profiles. Lines L07, L08, L10, L20, and L24, which are located at 7, 8, 10, 20, and 24 m from the origin (see Figure 3), were selected as representative of the area. The high resistivities observed in all profiles are caused by low moisture contents in the soil. Anomalies with lower resistivities are marked by ellipses in Figure 4. Note that anomalies labeled with the letter A are aligned along the profiles, although in L07 there is a slight displacement to the west. Anomaly A, located around 11 m, is related to the exposed wall, which was visible from approximately 4 to 16 m (east-west direction), as shown in Figure 2. Results in Figure 4 indicate this wall was at least 24 m long.

Similar but smaller anomalies near position 14 m, noted as B in Figure 4, could indicate the presence of another buried wall. Because the resistivity values were similar to A but the anomaly dimensions were smaller, it could indicate a narrower or more poorly preserved wall. In contrast, the other isolated anomalies in the figure (not identified with letters) differ from the response at A in that they do not continue from line to line.

Figure 5 shows models along four profiles obtained from the inversion of data acquired on east-west lines T09, T10, T11, and T12 located at 9, 10, 11, and 12 m from the origin, respectively. Once again, we can see lower-resistivity anomalies in very resistive matrices. Two groups of aligned anomalies can be observed at positions 9–10 m (anomaly C) and 16–17 m (anomaly F) in lines T09, T11, and T12 and to a lesser extent in T10. Anomalies D, E, H, and I appear as groups with shorter extensions. Given the exposed wall corresponding to anomaly A in Figure 4, we speculate the existence of buried walls that transversely intersect the exposed wall related to the observed anomalies in the T profiles.

If Figure 4 and 5 are analyzed together, we see there are matching anomalies in the south-north/east-west profiles. For example, an anomaly located at 10 m on line L10 (Figure 4) correlates with an anomaly found in profile T10 at 10 m (Figure 5). The compatibility of these results reinforces the possibility of delineating a buried structure at that position.

GROUND-PENETRATING RADAR

Field data

The GPR data were collected with a portable one-channel system produced by Ingegneria dei Sistemi S.P.A. (IDS). Adequate penetration and vertical resolution were achieved with a 400-MHz antenna. Forty traces per meter were acquired, each having 256 data samples and a total duration of 60 ns (time interval of 0.234 ns). The lines determined an orthogonal 1×1-m grid, which coincided with the grid used for the resistivity profiles. The labeling convention used for both methods is the same (see Figure 3).

A set of filters, applied in a four-step series described below, was designed to improve signal viewing. Once we determined the air-ground interface on the acquired radar section, we performed high-pass filtering along the profile direction to remove the direct waves, which completely hid approximately 50% of the range including the events of interest. Next we applied a smooth band-pass filter verti-

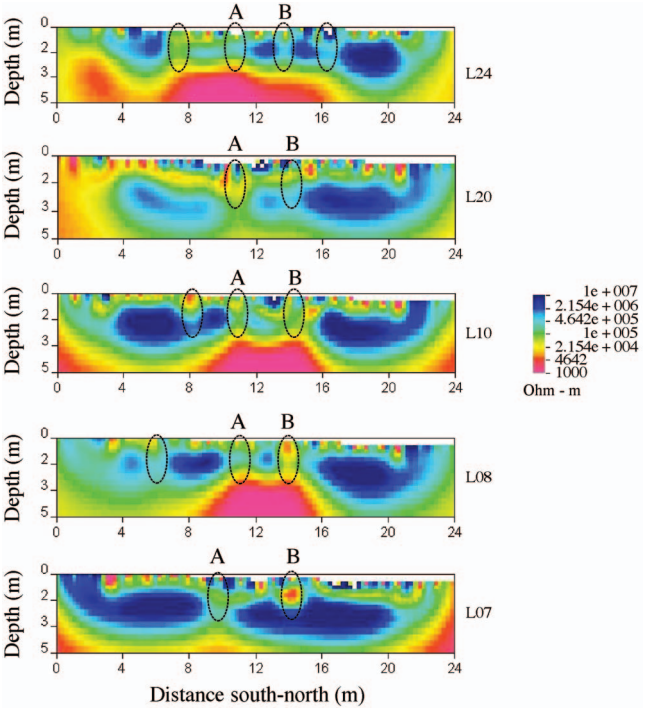

Figure 4. Electrical resistivity images obtained from 2D inversion of the dipole-dipole data along longitudinal lines L07, L08, L10, L20, and L24. Anomalies are located with dashed circles. Letters identify the anomalies attributed to buried walls.

cally in the [0.2, 1.0] GHz range, thus eliminating a large amount of high-frequency noise that was distributed outside the useful band of the signal. Finally, because of the attenuation of the signal with depth, we equalized trace amplitudes to obtain a better view of deep reflectors. We obtained the equalization factors from a smooth curve fit performed on the values of the rms average trace. If necessary, we applied a band-pass filter along the profile direction to remove pseudohorizontal disturbances. This procedure was used to highlight weak diffraction signals attributed to potential archaeological reflectors. These processes enabled a clear visualization of the main events, generating an immediate in-situ radargram. Figure 6 shows the processed data for lines L12, T09, T11, and T14, the direction being south-north for the first one and west-east for the last three.

Although these radargrams present many responses related to diffraction events, more intense and coherent signals occur in L12 and T11. These signals are identified as inverted V-shapes with truncated vertices. The two branches of such a response can be located in L12 from (D, t) (9.5 m, 1 ns) to (6.4 m, 35 ns) and from (D, t) (10.0 m, 1 ns) to (12.4 m, 27 ns), where D is the distance from the origin of the survey. This response, labeled A, is recorded by the radar when it orthogonally crosses the superior edges of the exposed wall (Figure 2); hence, it could be considered a characteristic response for a buried wall. Another similar but weaker signal can be observed in radargram L12; the top of the signal is located between positions (D, t) (12.0 m, 2 ns) and (12.4 m, 2 ns) (B in Figure 6). The qualitative analogy between this signal and the characteristic response of a wall leads us to infer another buried wall at this position.

We identified signals similar to the ones described above in most of the NH3 radargrams. For instance, in line east-west T11, three truncated V-shaped signals can be seen: the first from (D, t) (8.6 m, 2 ns) to (8.9 m, 2 ns) and two weaker ones from (D, t) (1.3 m, 1 ns) to (1.8 m, 1 ns) and from (D, t) (5.8 m, 2 ns) to (6.2 m, 2 ns), labeled C, G, and H, respectively. Toward the east end of the survey between (D, t) (12.6 m, 3 ns) and (13.1 m, 3 ns), the top of a fourth characteristic signal can be partially observed (E). Consequently, we predict buried walls at the mentioned locations. Note that no truncated V-shaped signals appear in radargrams T09 and T14, which are positioned at both sides of T11, so the aforementioned walls would be limited between them. More localized and simple signals with vertices at (D, t) (2.3 m, 2 ns) on T09 and at (3.7 m, 3 ns) on T11 can be attributed to small-size bodies. This kind of body generates intense and acute signals at shallow depths, i.e., complete inverted V-shaped signals without truncation can be seen from an estimation of the traveltime of the signal as a function of the source-receiver position on the surface for a compact, buried target.

Diffraction responses attributed to typical archaeological objects were designated archaeological GPR anomalies in contrast to GPR anomalies because of natural structures, considered as secondary events, attributed to clods, stones, natural faults, vegetal roots, etc. Signals that could not be clearly classified as archaeological or natural were considered as potentially archaeological.

An average velocity of the electromagnetic waves propagating in the media around the predicted walls was deduced from diffraction

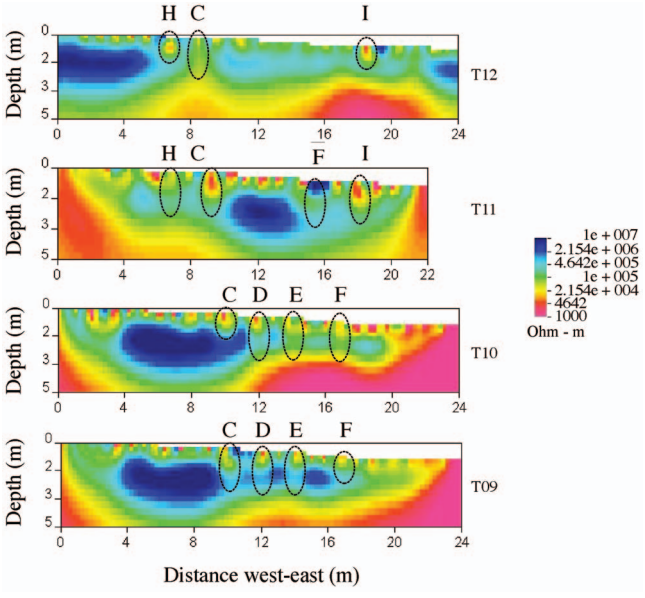

Figure 5. Electrical resistivity images obtained from 2D inversion of the dipole-dipole data along transverse lines T09, T10, T11 and T12. Anomalies are located with dashed circles. Letters identify the anomalies attributed to buried walls.

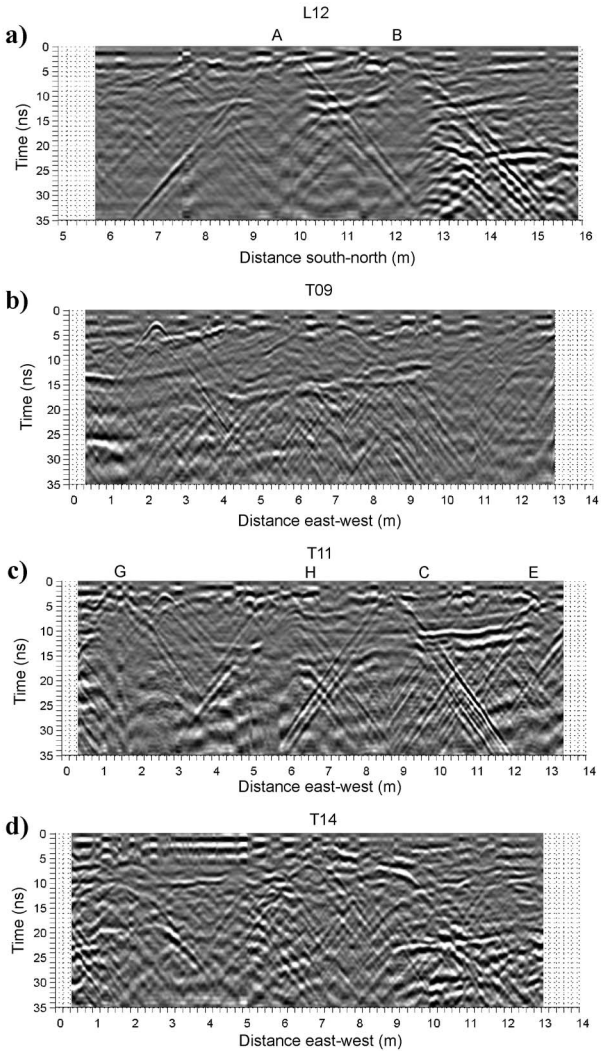

Figure 6. Radargrams along lines L12, T09, T11 and T14. Signals attributed to buried walls were identified with the same used to identify dipole-dipole anomalies.

tails as $V = 19.3\ (\pm 1.2)$ cm/ns. Depths to the tops of the walls and the shallower strata could be estimated from V and the two-way traveltimes. For example, in radargram T11, the tops of the predicted walls were established to be shallower than 0.2 m, whereas the reflection that occurs at $t4$ ns, between 4 and 4.2 m, was predicted at a depth of 1.2 m.

The foundations of predicted walls were not clearly visible in the data, so it was necessary to follow an indirect procedure to estimate their depths. We evaluated the continuity of the signals reflected at the most superficial strata; if a stratum clearly crosses through the range in which a wall has been located, the foundation of the wall must be shallower than that of the stratum. In this way, we obtained a crude estimate limiting the depth of the foundation of the wall. Subsequently, an average velocity for waves propagating within the wall is calculated by computing the time of the reflection at this stratum in the zone where the wall is located and using the estimated depth of the stratum. In some cases, this was successful; in many other cases, we could not determine if strata continued through a wall location because of interference and other phenomena discussed below.

Synthetic radargrams

To generate synthetic radargrams, a computer program originally developed by Carcione (1996) was adapted for a monostatic array. Based on a pseudospectral method in space, it uses the fourth-order Runge-Kutta formulas for field evolution along time, evaluates spatial increments through differential operators in the wave vector domain, and then retrieves the spatial distribution.

To help in identifying the nature of the recognized anomalies, synthetic signals were generated and compared to the measured responses. This comparison contributed to distinguishing the expected reflection events from others. The procedure was particularly useful when those events became complicated with secondary events because both signals could have comparable magnitudes. In the case of walls, this was mainly because of the low contrast (approximately less than 15%) between the average permittivities of the adobe and the sediments, as compared to natural fluctuations within the sediments of 40%, values which were obtained from inverted resistivities and average velocities.

Synthetic radargrams were used not only in the initial event-recognition stage but also later to check interpretations, before designing the excavation. In this stage, the synthetic radargrams were compared with the measured ones to check the results obtained from the analysis of profile data and the anomaly maps. Consequently, the models were constructed using the predicted locations and physical parameters for the archaeological anomalies and the surrounding soils and sediments.

In Figure 7a we show an interpreted model for line T11. The widths used for the walls of lines G, H, C, and E were 0.75, 0.85, 0.70, and 0.70 m, respectively. To obtain more realistic results, the edges of the walls were shaped to simulate the effects of erosion. The tops of the walls were located at a mean depth of 0.10 m and the foundations at 0.85 m for the first wall (G) and 0.55 m for the remaining walls. The depth of the foundation of wall E could not be estimated from the analysis of radargrams, so a typical value was used. A stratum with a depth of 1.27–0.83 m was also included. The relative permittivity values were 2.42, 2.58, and 2.83 for the sandy soils, the deeper sediments, and the walls, respectively. The lowest velocity values were obtained from the deepest diffractors. Resistivity values were estimated from the inverted resistivity profiles: 50,000 ohm-m for the sediments and 1250 ohm-m for the walls. A value of 5% noise in permittivity and resistivity parameters was included. Figure 7b shows the resultant radargram. The direct wave was removed and traces equalized, as explained previously.

Comparing field data to synthetic data in Figure 7b and c, respectively, we note a good correspondence in the spatial and temporal locations of the relevant events, as well as a qualitative correspondence in the relative amplitudes of the events, thereby attributing a degree of reliability to the interpreted model. However, some coincidences and differences between both kinds of radargrams should be mentioned and analyzed. In the synthetic radargram, the responses at the foundations of the walls are clearly visible, as indicated by the white arrows, although in the data there are no responses that could be unequivocally linked to the wall foundations. Furthermore, the continuity of the underlying strata through the predicted walls could be established only in relation to walls C and H, as denoted by white arrows in Figure 7c. Consequently, values for the depth can be attained only in these cases.

Difficulties in identifying the signals corresponding to the foundations of the walls can be caused by the following. First, the low permittivity contrast is minimized at the bases of the walls because of a slight increase in permittivity of the sandy medium with depth and the smooth transition within the mix of materials when walls were constructed. Second, frequency dispersion in the walls slightly dilutes the signals that propagate within them. Finally, for interfaces at less than 70 cm, the reflected signal tends to be masked by the tail from the signals coming from the tops of the walls. Another difference between the measured and the synthetic radargrams is the lack

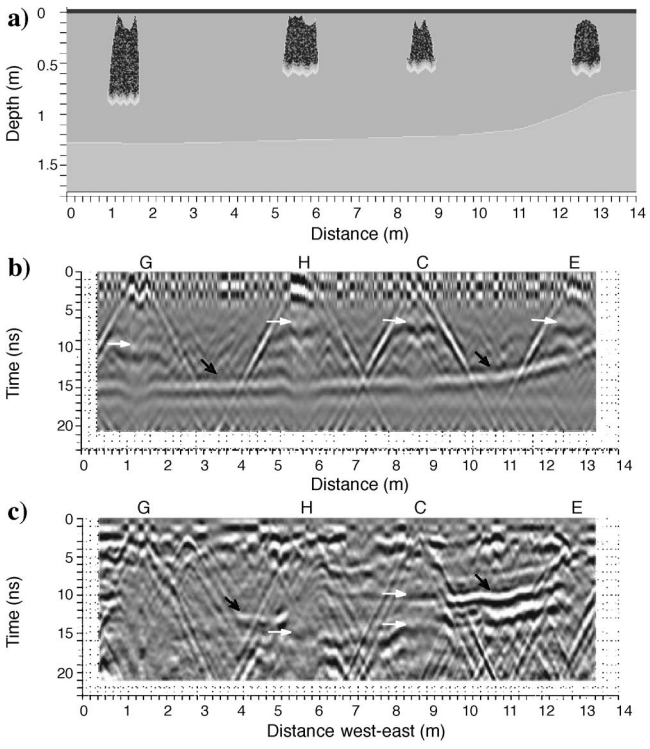

Figure 7. (a) Synthetic model for line T11. (b) Synthetic radargram corresponding to the model in (a). (c) Radargram T11. White arrows indicate the continuity of the underlying strata through the predicted walls. Black arrows point to a reflection in a deep strata. Differences between the figures are discussed in the text.

of coherency along consecutive traces in the most superficial area of Figure 7b (~5 ns). This comes from the fact that the noise applied to the synthetic radargram is random, which causes some abrupt variations in permittivity for lateral displacements on the order of 1 cm, the size of the horizontal increment in the program grid, similar in magnitude to those taking place at the top of the walls. Finally, discrepancies between the synthetic and field data in arrival times from the deep strata (pointed out with black arrows), especially from 9.5 to 12.6 m, are because of a misplacement in the synthetic model.

RESULTS

It is clear that considering the anomalies derived from dipole-dipole resistivity or GPR methods independently could result in incorrect predictions. Hence, complementary use of both methods becomes crucial. On a site map, we plotted resistivity anomalies in Figure 8a and GPR anomalies in Figure 8c. We believe it is likely that the coincident anomalies define a buried archaeological structure.

Failure to detect an anomaly is frequently linked to limitations inherent to the method. In areas where the tops of the walls have been cut and rounded by erosion, more diffuse and smoother GPR signals can be expected rather than those from sharp boundaries. This kind of signal may be attributed to factors not related to the wall but to local fluctuation in soil composition. Consequently, some omissions may be made when attempting to delineate the walls, which increases the risk of misinterpreting continuity of GPR anomalies. This happened with the wall located at approximately 1.7 m in the south-north direction, the signal of which was not identified in radargram T14 (Figure 6). We were able to overcome the misinterpretation of the discontinuity by favoring the correct identification of the wall (Figure 8a) determined by the resistivity model. This wall was especially significant in calculating the total surface of the dwelling area and therefore assessing time and cost of excavation.

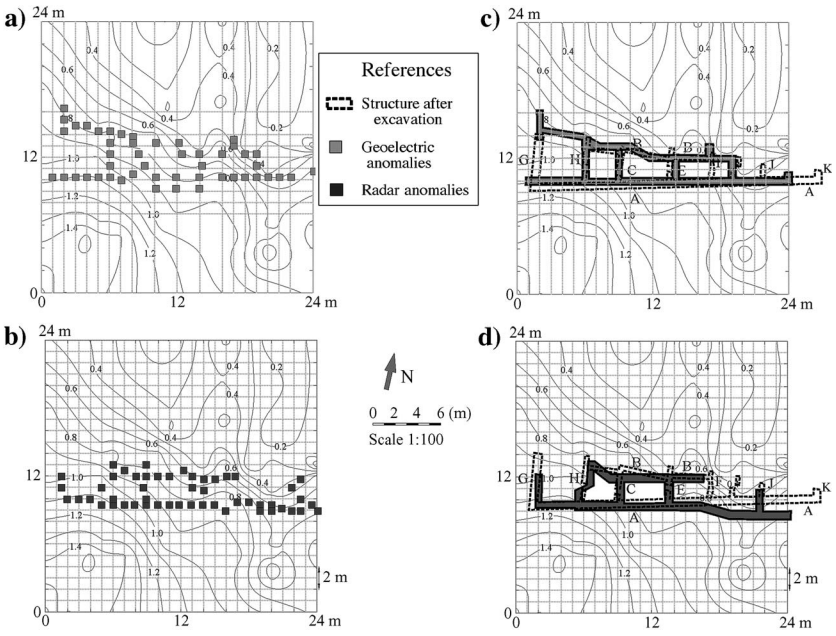

Figure 8. Maps of the predicted walls (a) obtained from the analysis of resistivity anomalies, (b) interpolated resistivity anomalies, (c) radar anomalies, and (d) interpolated radar anomalies. The position of the structure exposed from the excavation is shown with dotted lines. Walls are identified with letters to help with comparisons of the previous figures.

In turn, the resistivity method may miss detection of some buried anthropological structures — for instance, when the average resistivity of the structure is not significantly different from that of the soil and sediment. It is worth remembering that the people who lived at the site built the walls with clay material extracted from the same area. As a consequence, it is possible that geoelectric data along line T12 do not reveal the wall, even though it can be seen with GPR. Once again, an isolated analysis of either method would have failed to detect the wall because of a lack of continuity of the pertinent indicator.

Predictions from the analysis of anomalies were used to create a map of the site in Figure 8b and 8d for resistivity and GPR anomalies, respectively. A very interesting result is that the predicted structure is much more complex than that originally expected and, in fact, is more similar to the other structures shown in Figure 1b. This map was used for planning the subsequent excavation. The contours of the exposed structure after excavation were superimposed on the interpreted maps in Figure 8b and 8d with good agreement between the predicted and excavated structures. In the GPR anomaly map, the wall from E to K was south of that predicted. In the dipole-dipole interpretation, extensions of walls G and F were predicted north of the structure, and a buried wall was predicted between walls G and H at ~14 m. It was observed during excavation that these predicted walls were in fact clay blocks, originated from water erosion, mud flows, and detachments of materials from the walls.

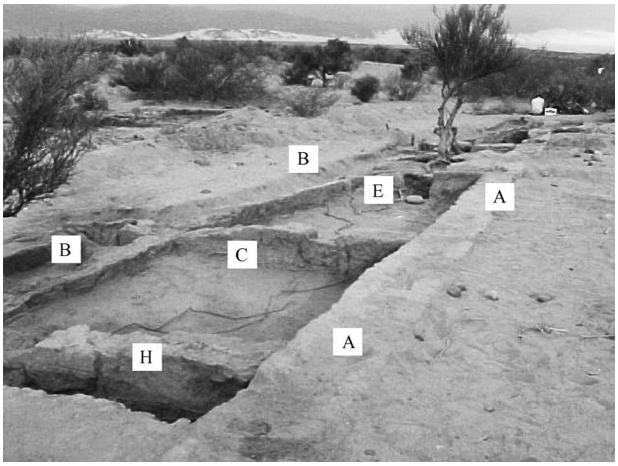

Figure 9. The site after excavation. Letters identify the anomalies corresponding to the exposed walls.

This map in Figure 8 was used to define strategies for the archaeological excavation, thereby ensuring that the walls could be preserved. Figure 9 shows a photograph after a partial excavation. The layout of the rooms fully matched the predictions based on the interpretation detecting the walls and their depths. This information is especially interesting to infer how the inhabitants moved from one room to another and to the outside. Also, pieces of pottery and evi-

dence of cooking activities were found within the structure, confirming human occupancy. The influence of the river seems to have impaired the area north of the house where part of the outer wall appears damaged. The determination of whether this event was the reason why the site had been abandoned is still pending.

CONCLUSIONS

Both the shallow-resistivity and GPR methods allowed us to identify anomalies that were subsequently interpreted as walls belonging to the archaeological unit of interest. Processing data resulted in clear images of the subsurface in which geoelectric and GPR anomalies could be interpreted through comparison with characteristic signals produced by an exposed wall. The procedures were successful even in cases in which the adobe of the walls and the surrounding materials presented low resistivity and permittivity contrasts. Numerical GPR simulations aided in the interpretation and confirmed wall location as well as width and depth estimates.

Using complementary methods played an important role in interpreting data and delineating the structural layout of the building foundation. The resistivity values obtained by inverting the dipole-dipole field data were necessary to refine the models for the GPR simulations. The GPR results established subsurface interpretation with a higher degree of reliability. Both methods failed to detect anomalies of interest because of the geometries and makeup of the sediments relative to the buried walls. In these cases, one method detected anomalies the other missed. Therefore, the complementary analysis made it possible to obtain a detailed map of the walls, which would have been incomplete if we had only used one of the methods.

ACKNOWLEDGMENTS

This work was supported by Fundación Antorchas and ANPCyT. We thank Mario Quintar, a municipal representative of Palo Blanco, for his technical assistance.

REFERENCES

Ambos, E. L., and D. O. Larson, 2002, Verification of virtual excavation using multiple geophysical methods: Case studies from Navan Port, County Amagh, Northern Ireland: The Society for American Archaeology, Archaeological Record, **2**, 32–38.

Blanton, R., 1994, Houses and households: Plenum Press.

Carcione, J., 1996, Ground radar simulation for archaeological applications: Geophysical Prospecting, **44**, 871–888.

Gordillo, I., 1999, Problemas cronológicos del Período Medio en el noroeste Argentino (in Spanish): Actas del XII Congreso Nacional de Arqueologa Argentina, **2**, 362–371.

Herbich, T., K. Misiewicz, and O. Teschauer, 1997, Multilevel resistivity prospecting of architectural remains: The Schwarzach case study: Archaeological Prospection, **4**, 105–112.

Hillier, B., and J. Hanson, 1984, The social logic of space: Cambridge University Press.

Loke, M. H., and R. D. Barker, 1996, Rapid least-squares inversion of apparent resistivity pseudosections by a quasi-Newton method: Geophysical Prospecting, **44**, 131–152.

Oldenburg, D. W., and Y. Li, 1994, Inversion of induced polarization data: Geophysics, **59**, 1327–1341.

———, 1999, Estimating depth of investigation in dc resistivity and IP surveys: Geophysics, **64**, 403–416.

Oldenburg, D. W., P. R. McGillivary, and R. G. Ellis, 1993, Generalized subspace method for large-scale inverse problems: Geophysical Journal Internacional, **114**, 12–20.

Osella, A., M. de la Vega, and E. Lascano, 2005, Floridablanca archaeological site: 3D electrical imaging study: Geophysics, **70**, 101–107.

Sempé, M. C., 1976, Contribución a la arqueología del valle de Abaucán, (in Spanish): Ph.D. thesis, La Plata University.

———, 1977, Las culturas agroalfareras prehispánicas del valle de Abaucán (Tinogasta-Catamarca) (in Spanish): Relaciones de la Sociedad Argentina de Antropología, **11**, 55–68.

Thacker, P. T., and B. B. Ellwood, 2002, Detecting palaeolithic activity areas through electrical resistivity survey: An assessment from Vale de Óbidos, Portugal: Journal of Archaeological Science, **29**, 563–570.